Journal of Materials Chemistry A

RSC Publishing

PAPER

View Article Online
View Journal | View Issue



Cite this: *J. Mater. Chem. A*, 2013, **1**, 10300

# The facile 3D self-assembly of porous iron hydroxide and oxide hierarchical nanostructures for removing dyes from wastewater†

Jinbo Fei, Jie Zhao, Cuiling Du, Hongchao Ma, He Zhang and Junbai Li*

Received 17th May 2013
Accepted 14th June 2013

DOI: 10.1039/c3ta11938f

www.rsc.org/MaterialsA

We report the template-free fabrication of 3D iron hydroxide hierarchical nanostructures through a simple and low-cost self-assembly process using a galvanic-cell reaction at room temperature. The existence of sodium sulfate in the reaction system is critical for formation of the iron hydroxide hierarchical nanostructures. X-ray diffraction analysis reveals that, after calcination, the iron hydroxide nanostructures can be changed into magnetic iron oxides. Relevant scanning electron microscopy and transmission electron microscopy images show that both of the flower-like nanostructures are composed of porous nanosheets. We also demonstrate that the two hierarchical nanostructures described above are negatively charged when dispersed in water. When used as adsorbents, they can selectively remove neutral dyes from wastewater with much higher capacities than those of conventional α-FeOOH and α-$Fe_2O_3$ nanoparticles, indicating great potential for use in water treatment.

## Introduction

Transition metal hydroxide and oxide nanostructures have been used for environmental protection because of features such as their rich valence states, vast surface areas and variable electronic structures.[1–10] Among these, iron oxide nanostructures such as nanoparticles, cubes, rods, wires, tubes, and sheets have all been extensively studied for use in water treatment.[11–24]

Up until now, hierarchical nanostructures have attracted much attention due to their unique physiochemical properties and potential applications.[25–29] However, self-assembly of the basic building blocks into well defined 3D nanostructures is still difficult.[30–34] To date, it has been a big challenge to develop simple and efficient synthetic methods for the hierarchical self-assembly of architectures with excellent properties.

Herein, we introduce a template-free preparation of novel 3D flower-like porous iron hydroxide and oxide nanostructures through a simple self-assembly process, referred to as a salt-assisted galvanic-cell reaction, at room temperature. As shown in Fig. 1, with the assistance of oxygen in air, iron alloy in ammonium sulfate aqueous solution can be oxidized to form iron hydroxide nanostructures. After calcination, the iron hydroxide nanostructures can be transformed into magnetic iron oxide nanostructures. The relevant reactions are as follows:

$$4Fe + 3O_2 + 2H_2O \rightarrow 4FeOOH$$

$$2FeOOH \rightarrow Fe_2O_3 + H_2O$$

Both nanostructures have good abilities for removing organic dyes from wastewater.

## Results and discussion

In a typical experiment, a 3 g iron nail entangled in copper wire was put into an aqueous solution of ammonium sulfate for 10 days at room temperature (about 20 °C). Noticeably and gradually, the surface color of the iron nail changed from a metallic luster to yellow and the relevant structure varied from fine and close, to loose (see Fig. S1†). Scanning electronic microscopy (SEM) and transmission electronic microscopy (TEM) were used to study the morphology of the precursor, as shown in Fig. 2. In detail, from Fig. 2A, one can see that particles were synthesized. Fig. 2B demonstrates that the diameter of the flower-like hierarchical precursor composed of nanosheets is about 200 nm

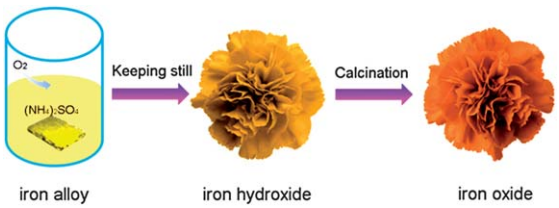


**Fig. 1** Schematic illustration of the construction of the iron hydroxide and oxide hierarchical nanostructures.

*Beijing National Laboratory for Molecular Sciences (BNLMS), Institute of Chemistry, Chinese Academy of Sciences, Beijing, 100190, China. E-mail: jbli@iccas.ac.cn; Fax: +86-01-82612629; Tel: +86-01-82614087*

† Electronic supplementary information (ESI) available: The chemical structures of the two dyes, photographs and SEM images of the related products, Fig. S1–S7 and Table S1. See DOI: 10.1039/c3ta11938f

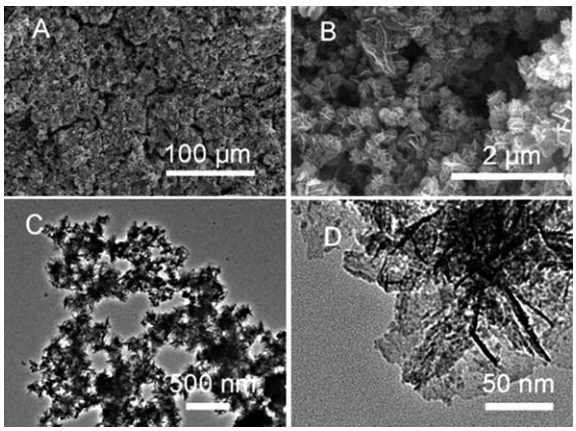


**Fig. 2** SEM images of the iron hydroxide nanostructures at (A) low magnification and (B) higher magnification; TEM images of the iron hydroxide nanostructures at (C) low magnification and (D) higher magnification.

and the thickness of the nanosheets is about 20 nm. Fig. 2C shows a similar result to Fig. 2B. Fig. 2D reveals that the precursor is porous, and therefore will have great potential to be used as an adsorbent.

From the results of energy diffraction X-ray (EDX) analysis (Fig. 3), one can see that there are three main elements in the precursor: Fe, O and Mn. This is because the iron nail used is an alloy. It should also be noted that the Si comes from the substrate used and the presence of Pt can enhance the conductivity of the samples. After calcination, there is no obvious change in the main elements. Furthermore, X-ray diffraction (XRD) spectroscopy was employed to investigate the phase transformation before and after calcination. Fig. 4A shows the reflection characteristics of the iron hydroxide hierarchical nanostructures, which matches well with the standard data of α-FeOOH (JCPDS no. 29-0713). In detail, the three main diffraction features appearing at about 21.2°, 36.6° and 53.2°, correspond to the (110), (111) and (221) planes of α-FeOOH, respectively. After calcination at 400 °C for 3 h, iron hydroxide can be changed into iron oxide (shown in Fig. 4B). In detail, the three main peaks between 35° and 65° are in good agreement with the (311), (400) and (440) planes of γ-$Fe_2O_3$ (JCPDS no. 39-1346). It can be concluded that iron hydroxide could be successfully transformed into iron oxide.

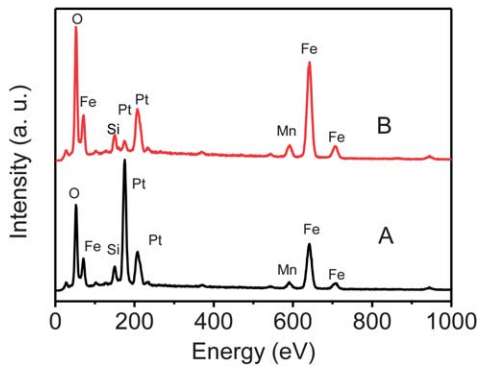


**Fig. 3** EDX patterns of (A) the iron hydroxide and (B) iron oxide hierarchical nanostructures.

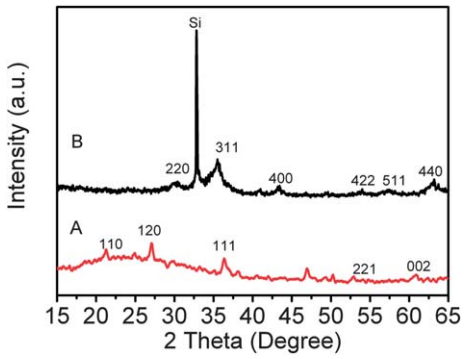


**Fig. 4** XRD patterns of (A) the iron hydroxide and (B) iron oxide hierarchical nanostructures.

Furthermore, SEM and TEM also were used to study the morphology of the iron oxide nanostructures. Fig. 5A shows that iron oxide can be prepared. Moreover, the morphology of the iron oxide nanostructures is similar to that of the iron hydroxide nanostructures (shown in Fig. 5B), indicating that they came from the precursor. In addition, Fig. 5C shows typical flower-like iron oxide hierarchical nanostructures. From Fig. 5D, the high resolution transmission electronic microscopy (HRTEM) image shows the phase characteristics of the iron oxide and the selected area electron diffraction (SAED) pattern (inset) shows the hierarchical nanostructures are polycrystalline. In a magnetic field, it is interesting that the iron oxide nanostructures, when dispersed in water, are attracted toward the magnet (shown in Fig. 6), which could be very helpful for cutting costs in the real operation of adsorbing waste.

In our previous reports, we used template-based methods to assemble manganese dioxide and iron oxide hierarchical nanostructures for use in water treatment.[10,12] In this communication, we have used two hierarchical nanostructures containing iron prepared using a template-free method to adsorb

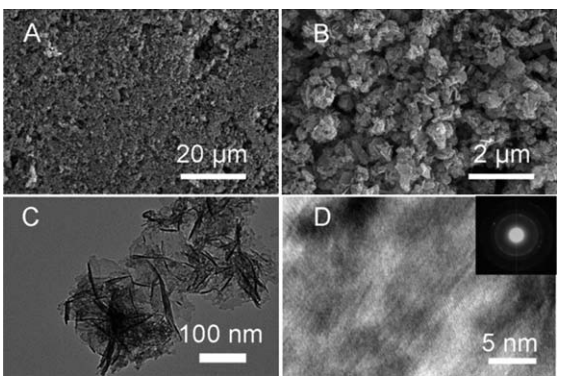


**Fig. 5** SEM images of the iron oxide nanostructures at (A) low magnification and (B) higher magnification; (C) TEM images of the iron oxide nanostructures; (D) HRTEM image of the iron oxide nanostructures, where the inset shows the relevant SAED pattern.

**Fig. 6** Photograph of the samples in a magnetic field. On the left is the iron hydroxide nanostructures and on the right is the iron oxide nanostructures.

organic dyes. In general, the larger the surface areas of an adsorbent the higher the capacity (see Table S1 in the ESI†).[35–41] It can be deduced that hierarchical nanostructures with large surface areas could result in good adsorption properties including a good capacity and an easy solid–liquid separation. In fact, the BET surface area of the iron hydroxide hierarchical nanostructures was 101.2 $m^2\ g^{-1}$, while that of the iron oxide hierarchical nanostructures was 114.5 $m^2\ g^{-1}$ (shown in Fig. 7A and B). This can be attributed to the formation of more pores during calcination. Additionally, the $N_2$ adsorption–desorption isotherms shown are consistent with the appearance of macropores. Moreover, before and after calcination, calculations from density-function-theory analysis showed that there were no obvious changes in the distribution of the average adsorption pore width (from mesopore to macropore). The zeta potentials of the precursor and product were about −4.14 and −2.18 mV, respectively, indicating that these two nanostructures could be used as absorbents to remove positively charged or neutral dyes. An aqueous solution of neutral Congo red was selected as a wastewater model, the chemical structure is illustrated in Fig. 8. It should be noted that after mixing, there was no change in the pH value for both of the hierarchical nanostructures. In addition, the maximum absorption peak of Congo red still appeared at about 500 nm, indicating that there was no chemical reaction during the adsorption process. Therefore, the characteristic absorption of Congo red at 500 nm was selected as the monitoring parameter for the adsorption process of the two hierarchical nanostructures. When the initial concentration of Congo red in the water solution was 100 mg $L^{-1}$, the as-obtained iron hydroxide and iron oxide were able to remove about 84.5% and 87.3% of the Congo red without the need for any additives at room temperature, as shown in the photographs and relevant UV-vis absorption curves plotted at different times (Fig. 9A and B). Furthermore, the relationship between the removal ability of the as-prepared samples and the concentration of the contaminated solution could be illustrated using the adsorption isotherm data (Fig. 10A). The Langmuir adsorption model was used for the adsorption analysis. Such a model was used to represent the relationship between the amount of dye adsorbed at equilibrium ($q_e$, mg $g^{-1}$) and the equilibrium solute concentration ($C_e$, mg $L^{-1}$):[42]

$$q_e = q_m b C_e/(1 + bC_e)$$

where $q_m$ (mg $g^{-1}$) is the maximum adsorption capacity corresponding to complete monolayer coverage and $b$ is the equilibrium constant (L $mg^{-1}$). Our results suggest that 1 g of the as-prepared iron hydroxide and oxide hierarchical nanostructures can remove about 56.3 mg and 58.2 mg of Congo red, respectively. It could be deduced that the larger surface area of the latter could bring about an enhancement of the adsorption capacity. In view of the characteristics of the surface charges, it can be inferred that the electrostatic attraction between the surface and the Congo red species in solution at pH 7.6 was responsible for the dye removal. In addition, as shown in

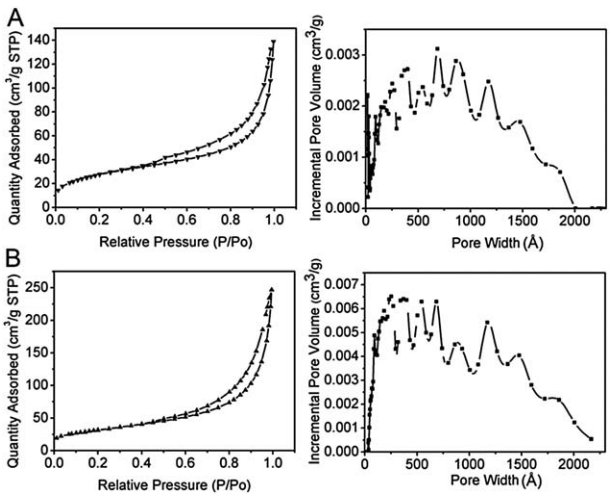


**Fig. 7** $N_2$ adsorption–desorption isotherms and a full range of pore size distribution curves for the two as-synthesized products; (A) the iron hydroxide and (B) iron oxide hierarchical nanostructures.

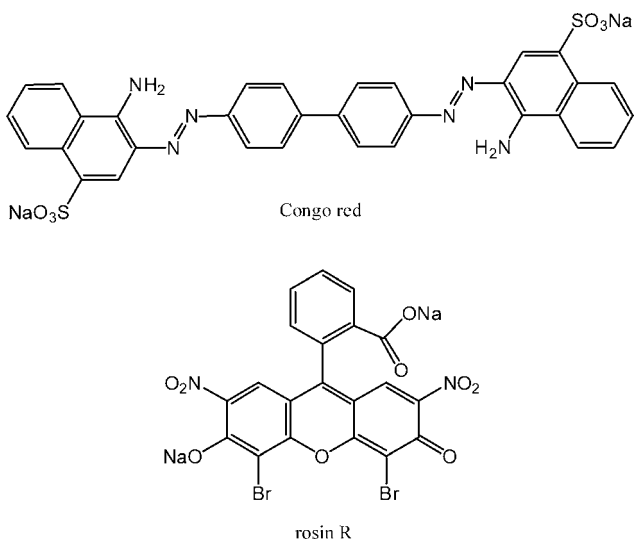


**Fig. 8** The chemical structures of Congo red and rosin R.

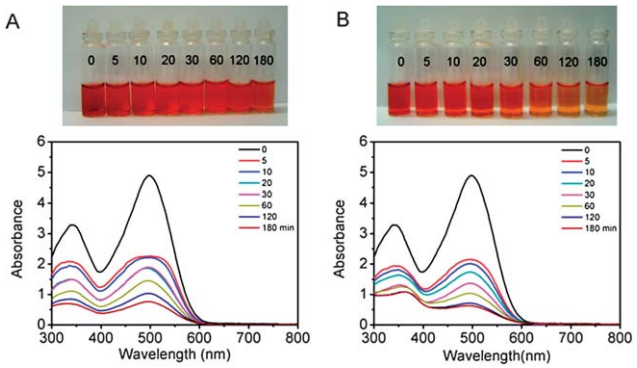


**Fig. 9** Photographs and time-depended adsorption curves (at 0, 5, 10, 20, 30, 60, 120 and 180 min, respectively) of (A) the iron hydroxide nanostructures and (B) iron oxide nanostructures obtained. The concentration of the Congo red solution was 100 mg $L^{-1}$. After centrifugation, the Congo red solutions were diluted to 20%.

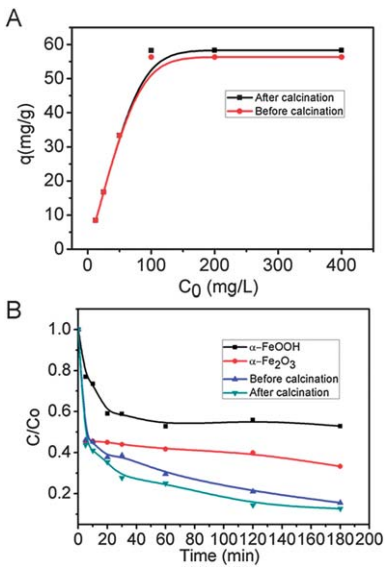


**Fig. 10** (A) Absorption isotherms of Congo red at different concentrations for the as-prepared samples before and after calcination. (B) Adsorption rate of Congo red on conventional α-FeOOH and α-$Fe_2O_3$ nanoparticles, and the iron hydroxide hierarchical nanostructures before and after calcination. $C_0$ (mg $L^{-1}$) is the initial concentration of the Congo red solution (100 mg $L^{-1}$, 20 mL) and $C$ (mg $L^{-1}$) is the concentration of the solution at different intervals during the adsorption.

Fig. 11, the nanostructures can adsorb and desorb Congo red many times by washing with ethanol without any obvious capacity decrease. So, it could also can be anticipated that the Congo red extracted with ethanol could be reused after distilling the solvent. As a comparison, conventional α-FeOOH nanoparticles were synthesized using direct deposition (see Fig. S2†). Usually the surface areas of the FeOOH nanoparticles prepared using the above method were between 30 and 98 $m^2$ $g^{-1}$.[38,43,44] In order to increase the surface area, special templates such as surfactants and small molecules needed to be used. From Fig. 10B, one can see that the capacities of the as-prepared nanostructures in this work are much larger than those of the conventional α-FeOOH and α-$Fe_2O_3$ nanoparticles (shown in

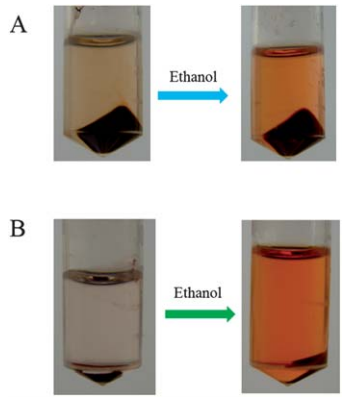


**Fig. 11** Photographs of (A) the iron hydroxide and (B) oxide hierarchical nanostructures adsorbing and desorbing Congo red.

Fig. S2†), which might be attributed to their larger surface areas and porous characteristics. Moreover, considering that the building blocks of the iron hydroxide and oxide nanostructures were connected to each other, it might be hoped that the solid and liquid would be readily separated for easy operation in real applications. In fact, after adsorption, the nanostructures spontaneously precipitate onto the bottom of flask used (as shown in Fig. S3A and 3B†). It should be noted that the surface charge of the nanostructures is critical for different kinds of adsorbed dyes. For instance, rosin R is negatively charged at pH 7. Its chemical structure is shown in Fig. 8. It can be hypothesized that it should not be adsorbed onto the two nanostructures described above. From Fig. 12, one can see that there is no obvious variation in colour after attempted adsorption for

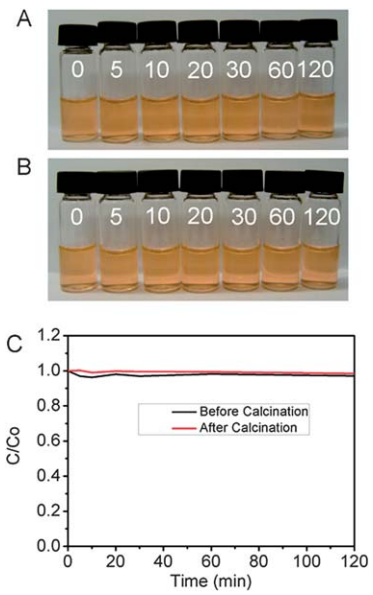


**Fig. 12** Photographs of adsorption of rosin R for the iron hydroxide hierarchical nanostructures (A) before and (B) after calcination. (C) Relevant adsorption rates of rosin R on two hierarchical nanostructures above. $C_0$ (mg $L^{-1}$) is the initial concentration of the rosin R solution (100 mg $L^{-1}$, 20 mL) and $C$ (mg $L^{-1}$) is the concentration of the solution at different intervals during the adsorption.

60 min. In addition, the accumulative adsorption percentages did not change even after attempted adsorption for 120 min.

## Conclusions

In summary, we have developed a simple template-free method, without using any additives to mimic natural corrosion processes, to construct porous ferric hydroxide and oxide hierarchical nanostructures. The addition of ammonium sulfate played a critical role in the synthesis of the iron oxide precursors. The approach described above can be referred to as self-assembly through limited heterogeneous chemical etching. Magnetic $\gamma$-$Fe_2O_3$ hierarchical nanostructures can be obtained from the precursor without changing the morphology by using a simple calcination procedure. The as-prepared iron oxide nanomaterials showed a good ability to remove dye pollutants in wastewater and are expected to be useful in many other applications.

## Experimental

In a typical procedure, 3 g of iron entangled in a copper wire was added to 50 mL solution of 0.2 M $(NH_4)_2SO_4$. The whole experiment was left open to the air. After 10 days at room temperature (20 °C), the as-synthesized iron hydroxide precursor was collected as a yellow precipitate using six centrifugation and ethanol washing cycles. All of the chemicals used (analytical reagents) were bought from Beijing Chemical Industry Group Imp. & Exp. Co. Water with an electronic resistance of 18.2 MΩ cm was used and provided by ELGA Labwater. Conventional $\alpha$-FeOOH nanoparticles were prepared using direct deposition according to the methods introduced in ref. 43 and 44. Common $\alpha$-$Fe_2O_3$ nanoparticles were bought from Alfa Aesar.

A Hitachi S-4800 scanning electron microscope (SEM) was used to investigate the morphologies of the precursors and final products. For the transmission electron microscopy (TEM) observations, the samples were re-dispersed in ethanol using an ultrasonic treatment and dropped on carbon–copper grids. TEM images were collected using a JEOL JEM 2010F microscope working at 200 kV. X-ray powder diffraction (XRD) measurements were carried out with a Rigaku D/max-2500 instrument using filtered Cu-K$\alpha$ radiation. A Hitachi U-3010 spectrophotometer was used to record the UV-Vis spectra of the various samples. BET analysis (Micrometrics ASAP 2020) was employed to obtain the Brunauer–Emmett–Teller (BET) specific surface areas of the samples through their nitrogen adsorption isotherms.

A taper flask (capacity *ca.* 150 mL) was employed as the reaction vessel. 30 mg of the adsorbent sample was added to a model system containing Congo red ($C_{32}H_{22}N_6O_6S_2Na_2$, Amresco Inc.) or rosin R (Amresco Inc.) solution (100 mg $L^{-1}$), with stirring. The adsorption isotherm was obtained by varying the initial Congo red concentration in the 20 mL volume and stirring for 12 h at room temperature (20 °C). UV-Vis absorption spectra were recorded at different intervals in order to monitor the process.

## Acknowledgements

We gratefully acknowledge financial support for this research by the Key Project of Knowledge Innovation Engineering of the Chinese Academy of Sciences (no. KZCX2-EW-410-02), the National Nature Science Foundation of China (no. 21007075 and 21021003), and the National Basic Research Program of China (973 program) 2009CB930101.

## Notes and references

1 Y. Tokura and N. Nagaosa, *Science*, 2000, **288**, 462.
2 A. Ohtomo and H. Y. Hwang, *Nature*, 2004, **427**, 423.
3 S. Thiel, G. Hammerl, A. Schmehl, C. W. Schneider and J. Mannhart, *Science*, 2006, **313**, 1942.
4 E. Dagotto, *Science*, 2007, **318**, 1076.
5 H. Y. Hwang, Y. Iwasa, M. Kawasaki, B. Keimer, N. Nagaosa and Y. Tokura, *Nat. Mater.*, 2012, **11**, 103.
6 J. B. Fei and J. B. Li, in *Nanomaterials for the Life Sciences*, ed. C. S. S. Kumar, Wiley-VCH, Weinheim, Germany, 2009, vol. 2, ch. 9.
7 J. B. Joo, Q. Zhang, I. Lee, M. Dahl, F. Zaera and Y. D. Yin, *Adv. Funct. Mater.*, 2012, **22**, 166.
8 J. B. Joo, Q. Zhang, M. Dahl, I. Lee, J. Goebl, F. Zaera and Y. D. Yin, *Energy Environ. Sci.*, 2012, **5**, 6321.
9 L. D. Zhang and M. Fang, *Nano Today*, 2010, **5**, 128.
10 J. B. Fei, Y. Cui, X. H. Yan, W. Qi, Y. Yang, K. W. Wang, Q. He and J. B. Li, *Adv. Mater.*, 2008, **20**, 452.
11 L. S. Zhong, J. S. Hu, H. P. Liang, A. M. Cao, W. G. Song and L. J. Wan, *Adv. Mater.*, 2006, **18**, 2426.
12 J. B. Fei, Y. Cui, J. Zhao, L. Gao, Y. Yang and J. B. Li, *J. Mater. Chem.*, 2011, **21**, 11742.
13 Y. Han, Y. J. Wang, L. Li, Y. P. Wang, L. F. Jiao, H. T. Yuan and S. X. Liu, *Electrochim. Acta*, 2011, **56**, 3175.
14 X. Huang, J. G. Guan, Z. D. Xiao, G. X. Tong, F. Z. Mou and X. A. Fan, *J. Colloid Interface Sci.*, 2011, **357**, 36.
15 S. L. Jin, H. G. Deng, D. H. Long, X. J. Liu, L. Zhan, X. Y. Liang, W. M. Qiao and L. C. Ling, *J. Power Sources*, 2011, **196**, 3887.
16 W. Zhang, J. Chen, X. Wang, H. L. Qi and K. S. Peng, *Appl. Organomet. Chem.*, 2009, **23**, 200.
17 Q. Y. Hao, S. Liu, X. M. Yin, Z. F. Du, M. Zhang, L. M. Li, Y. G. Wang, T. H. Wang and Q. H. Li, *CrystEngComm*, 2011, **13**, 806.
18 C. M. Cheng, F. J. Xu and H. C. Gu, *New J. Chem.*, 2011, **35**, 1072.
19 Y. Jung, Y. Son and J. Lee, *RSC Adv.*, 2012, **2**, 5877.
20 S. H. Sun and H. Zeng, *J. Am. Chem. Soc.*, 2002, **124**, 8204.
21 F. Lin and R. Doong, *J. Phys. Chem. C*, 2011, **115**, 6591.
22 C. T. Yavuz, J. T. Mayo, W. W. Yu, A. Prakash, J. C. Falkner, S. Yean, L. Cong, H. J. Shipley, A. Kan, M. Tomson, D. Natelson and V. L. Colvin, *Science*, 2006, **314**, 964.
23 H. Zeng, J. Li, J. P. Liu, Z. L. Wang and S. H. Sun, *Nature*, 2002, **420**, 395.
24 W. Yantasee, C. L. Warner, T. Sangvanich, R. S. Addleman, T. G. Carter, R. J. Wiacek, G. E. Fryxell, C. Timchalk and M. G. Warner, *Environ. Sci. Technol.*, 2007, **41**, 5114.

 

25 Y. Huang, X. F. Duan, Q. Q. Wei and C. M. Lieber, *Science*, 2001, **291**, 630.
26 H. T. Shi, L. M. Qi, J. M. Ma and H. M. Cheng, *J. Am. Chem. Soc.*, 2003, **125**, 3450.
27 U. Feldkamp and C. M. Niemeyer, *Angew. Chem., Int. Ed.*, 2006, **45**, 1856.
28 Q. G. Wang, J. L. Mynar, M. Yoshida, E. Lee, M. Lee, K. Okuro, K. Kinbara and T. Aida, *Nature*, 2010, **463**, 339.
29 T. Aida, E. W. Meijer and S. I. Stupp, *Science*, 2012, **335**, 813.
30 G. M. Whitesides and B. A. Grzybowski, *Science*, 2002, **295**, 2418.
31 D. A. Dikin, S. Stankovich, E. J. Zimney, R. D. Piner, G. H. B. Dommett, G. Evmenenko, S. T. Nguyen and R. S. Ruoff, *Nature*, 2007, **448**, 457.
32 S. Park, J. H. Lim, S. W. Chung and C. A. Mirkin, *Science*, 2004, **303**, 348.
33 G. M. Whitesides, J. P. Mathias and G. T. Seto, *Science*, 1991, **254**, 1312.
34 B. Pokroy, S. H. Kang, L. Mahadevan and J. Aizenberg, *Science*, 2009, **323**, 237.
35 C. Yu, X. Dong, L. Guo, J. Li, F. Qin, L. Zhang, J. Shi and D. Yan, *J. Phys. Chem. C*, 2008, **112**, 13378.
36 R. Rahimi, H. Kerdari, M. Rabbani and M. Shafiee, *Desalination*, 2011, **280**, 412.
37 Y. F. Zhao, S. He, M. Wei, D. G. Evans and X. Duan, *Chem. Commun.*, 2010, **46**, 3031.
38 B. Wang, H. B. Wu, L. Yu, R. Xu, T. T. Lim and X. W. Lou, *Adv. Mater.*, 2012, **24**, 1111.
39 B. Cheng, Y. Le, W. Q. Cai and J. G. Yu, *J. Hazard. Mater.*, 2011, **185**, 889.
40 J. H. Pan, X. W. Zhang, A. J. Du, D. D. Sun and J. O. Leckie, *J. Am. Chem. Soc.*, 2008, **130**, 11256.
41 Z. H. Wei, R. Xing, X. Zhang, S. Liu, H. H. Yu and P. C. Li, *ACS Appl. Mater. Interfaces*, 2013, **5**, 598.
42 R. C. Wu, J. H. Qu and Y. S. Qu, *Water Res.*, 2005, **39**, 630.
43 F. J. Hingston, A. M. Posner and J. P. Ouirk, *J. Soil Sci.*, 1974, **25**, 16.
44 L. A. G. Aylmore, *Clays Clay Miner.*, 1974, **22**, 175.